Available online at www.sciencedirect.com
SCIENCE DIRECT®
Journal of Electron Spectroscopy and Related Phenomena 141 (2004) 95–104
JOURNAL OF ELECTRON SPECTROSCOPY and Related Phenomena
www.elsevier.com/locate/elspec

The direct measurement of spectral momentum densities of silicon with high energy (e, $2e$) spectroscopy

C. Bowles, A.S. Kheifets, V.A. Sashin, M. Vos*, E. Weigold

Atomic and Molecular Physics Laboratories, Research School of Physical Sciences and Engineering, Australian National University, Canberra, ACT 0200, Australia

Received 31 March 2004; received in revised form 4 April 2004; accepted 5 May 2004
Available online 13 September 2004

Abstract

Electron momentum spectroscopy is a coincidence technique that measures the spectral momentum density of matter. In this paper we outline the theoretical framework underlying these measurements, give a description of the spectrometer, and show in detail the information this technique can provide for the prototypical material silicon. We present results for single crystals as well as amorphous samples, describe the influence that diffraction and inelastic multiple scattering have on these measurements. The results are compared with full-potential linear-muffin-tin-orbital (FP-LMTO) calculations (for dispersion), and many-body calculations (for line shapes).

PACS: 71.20.Mq; 79.20.Kz

Keywords: Spectral function; Electron momentum spectroscopy; Band structure; Silicon

1. Introduction

In a scattering experiment at high momentum transfer, where the projectile scatters from target electrons in binary collisions, one can determine a projection of the target electron momentum density by measuring only the scattered particle energy (and hence momentum) distribution. These so called Compton scattering studies can be done using either photons [1,2] or electrons [3]. There is no access to the complete momentum density, as no information is obtained on the momentum of the target electrons after the collision. If one uses thin films the target electron, having gained energy in the scattering event, will escape from the material and can be detected as well. Studies measuring the momentum of the scattered particle and that of the ejected electron in coincidence can thus determine directly the full momentum density. Using photons as probing particle this technique is either referred to as (γ, $e\gamma$) spectroscopy [4] or (X, eX) experiments [5].

The momentum distributions obtained in this way are those of the sum of all occupied orbitals. If one wants to access the momentum distribution of specific orbitals, one has to accurately determine the energy of the incoming and outgoing particles. For incident photons, the cross section is small and it has not yet been possible to have sufficient energy resolution to determine state-specific momentum densities within the valence band, although it has been possible to separate valence and core level momentum densities [5]. When electrons are used as the probing particles this technique is known as (e, $2e$) spectroscopy, or electron momentum spectroscopy (EMS) [6]. In EMS the cross sections are large enough that the spectral electron momentum density (SEMD) (or spectral function) $A(\boldsymbol{q}, \omega)$ can be measured with an energy resolution of around 1 eV and momentum resolution of 0.1 a.u. In an independent particle model $A(\boldsymbol{q}, \omega)$ is proportional to the probability that an electron has the momentum $-\boldsymbol{q}$ and energy ω. Examples of results of this technique are presented in this paper.

Denoting the energies and momenta of the incident and outgoing electrons respectively by E_0, E_1, E_2, and $\boldsymbol{k}_0$, $\boldsymbol{k}_1$ and $\boldsymbol{k}_2$, for each (e, $2e$) event one can determine the binding

* Corresponding author.
E-mail address: maarten.vos@rsphysse.anu.edu.au (M. Vos).

0368-2048/$ – see front matter © 2004 Elsevier B.V. All rights reserved.
doi:10.1016/j.elspec.2004.05.006

or separation energy of the ejected electron:

$$\omega = E_0 - E_1 - E_2, \tag{1}$$

and the recoil momentum $\boldsymbol{q}_r$ of the ionised specimen:

$$\boldsymbol{q} = \boldsymbol{k}_0 - \boldsymbol{k}_1 - \boldsymbol{k}_2. \tag{2}$$

The differential cross section is given by [6]:

$$\sigma(\boldsymbol{k}_0, \boldsymbol{k}_1, \boldsymbol{k}_2, \omega) = (2\pi)^4 k_0^{-1} k_1 k_2 f_{ee} A(\boldsymbol{q}, \omega). \tag{3}$$

Here f_{ee} is the electron–electron scattering factor, which is constant in the non-coplanar symmetric kinematics used in the spectrometer at the Australian National University [7,8]. Thus, the $(e, 2e)$ cross section is directly proportional to the SEMD. Further, since the measurements involve real momenta and the crystal momentum $\boldsymbol{k}$ does not appear in the expression for the cross section, EMS can also measure SEMDs for amorphous and polycrystalline materials.

The electronic structure of the ground state of a solid is described by its SEMD $A(\boldsymbol{q}, \omega)$. Only states with $\omega < E_f$ are occupied and will contribute to the measured intensity. Presuming that the Green's function can be diagonalised on an appropriate basis of momentum-space quasiparticle states $\phi_j(\boldsymbol{q})$, then for a crystal it takes the form [9]:

$$A(\boldsymbol{q}, \omega) = \sum\nolimits_{j,\boldsymbol{k},\boldsymbol{G}} |\phi_j(\boldsymbol{q})|^2 \delta_{\boldsymbol{q},(\boldsymbol{k}+\boldsymbol{G})} \frac{1}{\pi} Im G_j^-(\boldsymbol{k}, \omega). \tag{4}$$

Here $\phi_j(\boldsymbol{q})$ is the Fourier transform of the coordinate space wave function taken over the unit cell, $\boldsymbol{G}$ is a reciprocal lattice vector, and $G^-(\boldsymbol{k}, \omega)$ is the interacting single-hole (retarded) Green's function of the many-electron system. The interacting SEMD contains much more information than just the band dispersion. The main feature describes the probability of quasiparticle in band j having momentum $\boldsymbol{k}$ and energy ω. The quasiparticle peak is shifted with respect to the one-electron energy $\varepsilon_{j,\boldsymbol{k}}$ and it acquires a width due to the finite lifetime of the quasiparticle. In addition electron correlation effects can give rise to significant satellite structures. For the independent electron case $Im G_j^-(\boldsymbol{k}, \omega)$ simplifies to $\delta(\omega - \varepsilon_{j\boldsymbol{k}})$ with $\varepsilon_{j\boldsymbol{k}}$ the energy of the one-electron state in band j with crystal momentum $\boldsymbol{k}$.

The measurement of the full SEMD for a solid is therefore of great interest since it can be directly compared with fundamental theoretical predictions of the electronic behaviour of the solid. Different experimental techniques have been developed to look at different aspects of the SEMD. For instance, angle-resolved photo-electron spectroscopy (ARPES) can provide high resolution measurements of the energy dispersion of the outer occupied states in single crystals, i.e. the peak values of $A(\boldsymbol{q}, \omega)$, although it cannot give direct information on the intensity distribution of $A(\boldsymbol{q}, \omega)$[10].

In this paper we present some EMS measurements of the valence SEMD of the prototypical semiconductor silicon and compare the results with calculations based on the independent particle approximation and on many-body approximations to the interacting one-particle Green's function. In Section 2 we discuss briefly the experimental technique. The results for Si are given and discussed in Section 3.

2. Experimental details

The apparatus and experimental techniques are fully discussed in [7,8]. The EMS spectrometer is shown schemat-

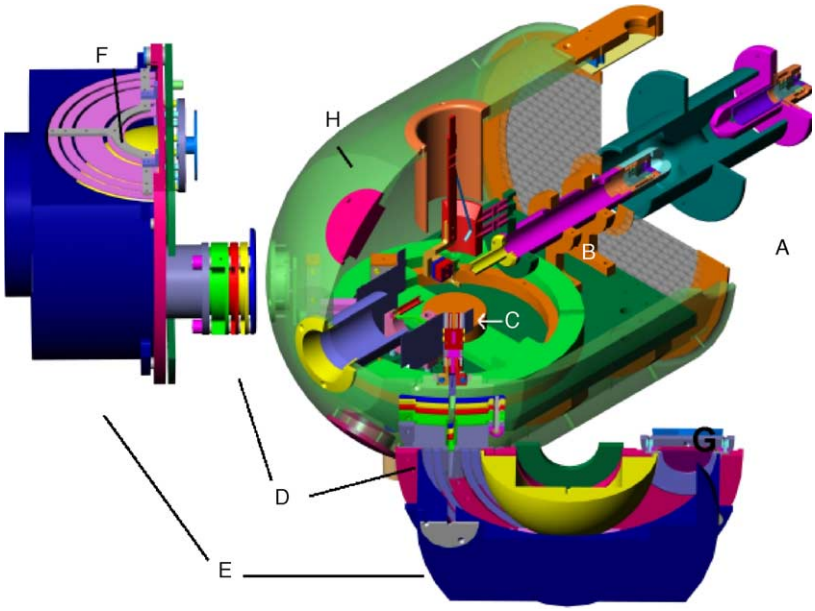

Fig. 1. Outline of the electron optics. The cathode of the electron gun (not shown) is at − 25 kV. Electrons enter the target area via the accelerator lens (A) and collimator (B). The target (C) can be positioned using a manipulator. Scattered and ejected electrons are decelerated by conical slit lenses (D) and enter the hemispherical analysers (E) with hoops for fringe field corrections (F) and detected by a channelplate/resistive anode detector (G). The target sample is mounted inside a hemisphere (H), both kept at +25 kV.

ically in Fig. 1. The sample is mounted on a manipulator in the centre of a hemisphere, all at high voltage (+25 kV). The electron gun cathode is at − 25 kV. Thus, a beam of 50 keV electrons, which is highly collimated, impinges on the thin self-supporting sample, the beam diameter being 0.1 mm. The kinematics is shown schematically in Fig. 2, the incident beam direction defining the z-axis, the mean scattering plane is the horizontal x–z-plane, with the y-direction being the vertical.

The emerging pairs of electrons with energies close to 25 keV are decelerated from the sample region to enter two symmetrically mounted hemispherical electrostatic analysers. Slits in front of the analysers only transmit electrons emerging along sections of a cone defined by $\Theta = 44.3^\circ$ (Fig. 2), which is chosen so that if all three electrons are coplanar then there is no momentum transferred to the target (i.e. $\boldsymbol{q} = 0$). If the electrons are not in the same plane (i.e. $\phi_1 \neq \phi_2$) then there is a y-component of momentum with $q_x = q_z = 0$, so only target electrons with momentum along the y-axis can cause a coincidence event. Two-dimensional position-sensitive detectors mounted at the exit planes of the analysers determine the energy and y-component of momentum of the transmitted electrons. The pass energy of the analysers is set so that electrons emerging in an energy window of 80 eV can be simultaneously detected, the azimuthal angular range being from -5° to $+5^\circ$. The long-term coincidence full-width-half-maximum energy resolution is 1.0 eV and momentum resolution is 0.1 a.u. [9].

Two pairs of deflection plates can be used to change the scattering angle θ of electrons entering the analysers by up to 1°. In this way one can select nonzero values for the x- and/or the z-component of momentum, so that the measurement along the y-direction (which ranges from − 5 up to +5 a.u.) can be chosen to slice through different regions of momentum space, making it possible to probe it fully in its three-dimensions. These deflectors can also be used to check and ensure that there are no offsets in q_x or q_z due to any small geometrical misalignments [7,11]. By observing the diffraction pattern of the transmitted electron beam on a phosphorescent screen, the alignment of the crystal direction chosen for study can be checked, and if necessary adjusted by means of the manipulator to line up the desired crystal direction with the y-axis of the spectrometer.

The preparation of the ultra-thin ($\simeq$ 10 nm) self-supporting single crystal targets is described in [7,8]. This is done under UHV in a separate target preparation chamber. The samples are then transferred to the spectrometer under UHV conditions. In addition we prepared films of amorphous silicon by evaporation of $\simeq$ 15 nm silicon on a 3 nm thick amorphous, free-standing carbon film. The carbon film was subsequently removed by sputtering with 600 eV Ar^+ ions.

Multiple scattering of the incoming or outgoing electrons can occur even with these thin samples and must be taken into account. Elastic collisions can change the momentum and inelastic collisions the energy of the high-energy electron, moving the $(e, 2e)$ event to 'wrong' parts of the energy–momentum space. These multiple-scattering effects can be modelled by Monte Carlo simulations in the case of polycrystalline or amorphous targets [12]. For single crystal targets the effects of elastic scattering adds coherently (diffraction). In that case diffraction changes of the incoming or outgoing electron momenta (and hence the recoil momentum, see Eq. 2) by a reciprocal lattice vector. The diffracted contribution can generally be disentangled from the main one [14,15], as will be shown in Section 3.3.

Quite generally, the inelastic events can be deconvoluted from the data by measuring an electron energy loss spectrum

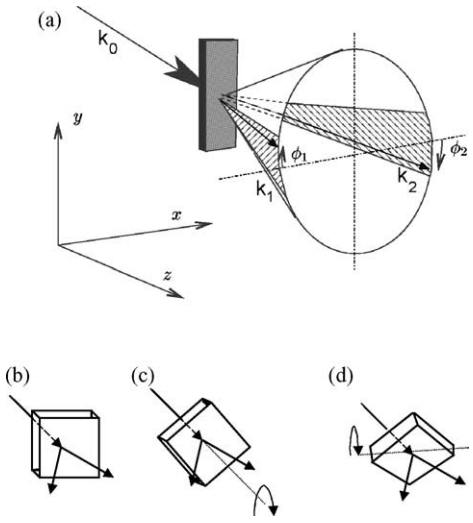

Fig. 2. Schematics of the kinematical arrangements. Electrons of momentum $\boldsymbol{k}_0$ incident along the z-axis eject an electron from a thin self-supporting single crystal of Si. The scattered and ejected electrons emerging along the shaded portions of the cone with half-angle $\Theta = 44.3^\circ$ are detected in coincidence by two angle and energy sensitive analysers. In this geometry we can only get coincidences for electrons with momentum along the y-axis. Measurement for different crystal orientations are done by rotating the crystal as shown in (b) ⟨1 0 0⟩ direction, (c) ⟨1 1 0⟩ direction and (d) ⟨1 1 1⟩ direction.

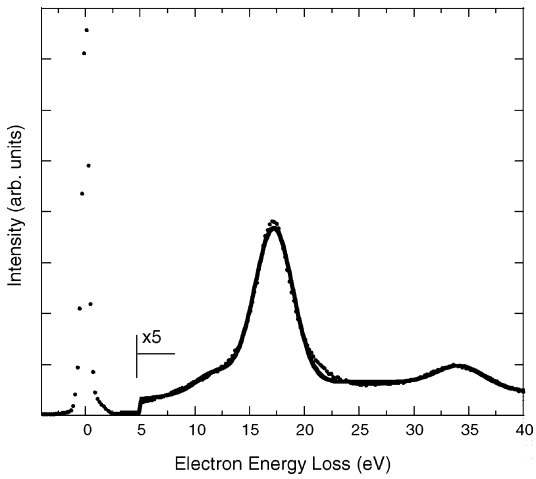

Fig. 3. The energy loss spectrum obtained for the 20 nm thick Si target with 25 keV incident electrons.

(EELS) for 25 keV electrons passing through the sample. This deconvolution, which is done without any free parameters [13], is carried out in the present case. Fig. 3 shows the energy loss spectrum for 25 keV incoming electrons obtained with one of the silicon crystal targets. The prominent energy loss feature at around 17 eV is due to the excitation of a plasmon, whereas the smaller peak centred around 34 eV is due to the excitation of two plasmons. In the EMS experiment both 50 and 25 keV electrons are involved. The type of inelastic excitations a 50 or a 25 keV electron can excite are very similar, but the mean free path (inversely proportional to the probability of an excitation per unit path length) of a 50 keV electron is longer than that of a 25 keV electron. As the relation between the probability of energy loss events in an EMS experiment and a 25 keV EELS experiment is known [13], we can use the EELS experiment to correct the EMS experiment for multiple scattering. The results of this deconvolution procedure, recovering the intrinsic line shape, is given in Section 3.4.

3. Results for silicon

3.1. Dispersion along different crystallographic directions

With the emitted electron deflectors set to ensure that the y-momentum range passed through $\boldsymbol{q} = 0$ (a Γ point), measurements were made along the crystal $\langle 1\,0\,0\rangle$ and $\langle 1\,1\,0\rangle$ directions (see Fig. 2b and c), and at four intermediate angles. For these measurements the crystal surface normal, the $\langle 0\,0\,1\rangle$ direction, was aligned with the z-direction and the crystal rotated about this direction as shown in Fig. 4. By tilting the crystal aligned along the $\langle 1\,1\,0\rangle$ direction by 35.3° as shown in Fig. 2(d), the $\langle 1\,1\,1\rangle$ direction was aligned with the y-axis and measurements taken. The results for the valence band region are shown in Fig. 5, where they are compared with some full-potential linear-muffin-tin-orbital (FP-LMTO) calculations [15]. The calculations were broadened by the experimental energy resolution of 1 eV and split up into the four occupied bands.

For the measurement along the $\langle 1\,0\,0\rangle$ direction the theory predicts that bands 1 and 2 are occupied. In the first Brillouin zone band 1 is occupied, changing abruptly to band 2 on crossing to Brillouin zone 2 at 0.61 a.u. (see Fig. 4) with no band gap. After leaving the second Brillouin zone the density drops only gradually to zero, a behaviour also shown by the measured density. This, however, also shows an additional branch at smaller binding energies, which merges with the main branch at 1.2 a.u. This additional branch appears in the calculated band structure in the case where the crystal has been rotated by 8.5°, and is due to band 4. Measurement along the $\langle 1\,0\,0\rangle$ direction just misses zone 4, so that due to finite momentum resolution (not included in the calculations) intensity will be picked up from this zone, giving rise to the extra branch in the measured density distribution.

In the $\langle 1\,1\,0\rangle$ direction the first Brillouin zone crossing is at the intersection of 2 planes (the (1 1 1) and (1 1 $\bar{1}$) planes) and hence it switches straight to zone 3. Here we see the classic band gap behaviour, band 1 having a minimum in binding energy at the crossing with its density petering out after the crossing. Band 3 slowly increases in intensity from zero momentum up to the first Brillouin zone boundary, where it has a maximum in binding energy, with density increased as one passes through Brillouin zone 3, and as it leaves zone 3 it has a minimum in binding energy. The calculations and the measurement are in quite good agreement for these general features. For the intermediate orientations all four bands contribute, band 1 remains dominant at small q and band 4

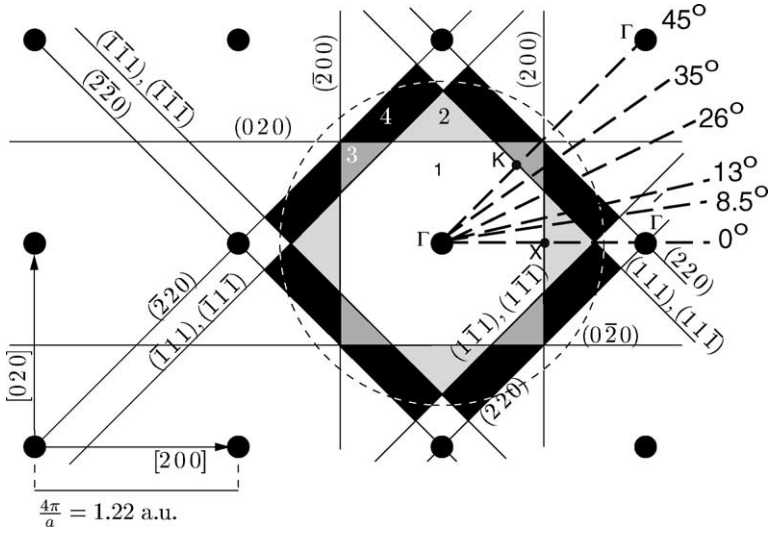

Fig. 4. The $q_z = 0$ plane of the reciprocal lattice of silicon with the first 4 Brillouin zones labelled. The Brillouin zone boundaries are labelled by the indices of the reciprocal lattice it bisects. The dashed circle indicates the Fermi sphere for a free electron solid with the same electron density as silicon. The dashed lines indicate the different measurements through the $\boldsymbol{q} = 0$ point (see Fig. 5). Different high-symmetry points of the reciprocal lattice are labelled by Γ, X and K.

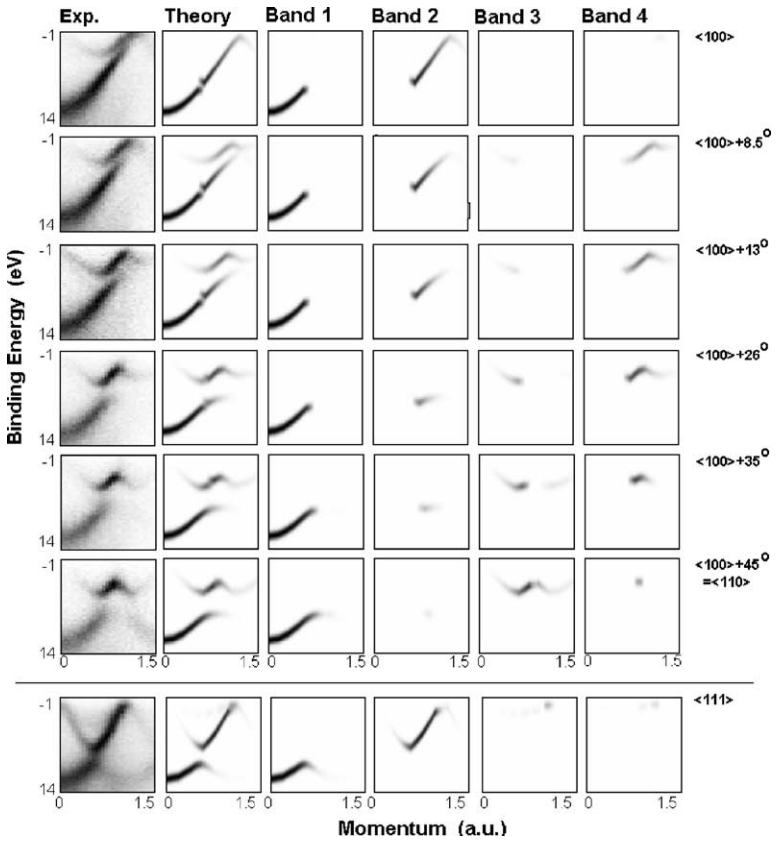

Fig. 5. The measured spectral momentum densities along different directions through the q = 0 point compared with FP-LMTO calculations (total plus separate band contributions).

becomes prominent at the larger q values. Also for these intermediate orientations the experimental results are again in quite good agreement with the calculated spectral momentum densities.

Note the correspondence between the calculated contributions of the different bands (1–4) in Fig. 5 and the the Brillouin zone picture in Fig. 4. If a certain momentum value is in Brillouin zone x, then band x is the major contributor to the intensity at that momentum value.

Along the ⟨1 1 1⟩ direction, reached by tilting the crystal as shown in Fig. 2d, the density is due to bands 1 and 2 with a large band gap at the zone crossing. Again the main features of the measurement are in agreement with theory, although the dispersion of the bands is mapped over a much larger range of momentum than given by the calculation. This is due to diffraction effects, which are discussed in detail in [11,15].

The dispersion obtained from a fit of the measurement is shown in Fig. 6 together with the calculated dispersion, based on the FP-LMTO theory, and some of the available photoemission data. In the bottom panel we show the calculated density of each band. Wherever a band has significant occupation, we could determine its dispersion. Again in the ⟨1 1 1⟩ case the dispersion could be tracked beyond the region with significant momentum densities due to diffraction.

3.2. Amorphous Si compared to single-crystal Si

Silicon films grown at room temperature are known to be amorphous, rather than crystalline. It is an important feature of EMS that it can resolve the spectral momentum densities of amorphous as well as crystalline materials. Amorphous silicon measurements were reported before using the Flinders University spectrometer (see [18]) but for this spectrometer there are no high-quality single crystal data available, as it requires extremely thin films. Here we want to compare the results of both amorphous and single-crystal films obtained with the ANU spectrometer. These measurements could help establish the validity of models of the electronic structure of amorphous materials as proposed by e.g. Ziman [19] or Hickey and Morgan [20].

The different character of the film is evident from the diffraction pattern observed at the phosphorous screen, as shown in Fig. 7. Most of the incoming beam does not interact elastically with the film, as it has a thickness less than the elastic mean-free-path length (about 40 nm for 50 keV electrons in Si). This causes the sharp main peak. However, there is a broad, low intensity, distribution under this sharp peak for the amorphous sample, and a broad distribution with additional sharp peaks for the crystalline one. These diffraction patterns illustrate how elastic scattering affects the incoming beam i.e. that the momentum of the incoming electrons

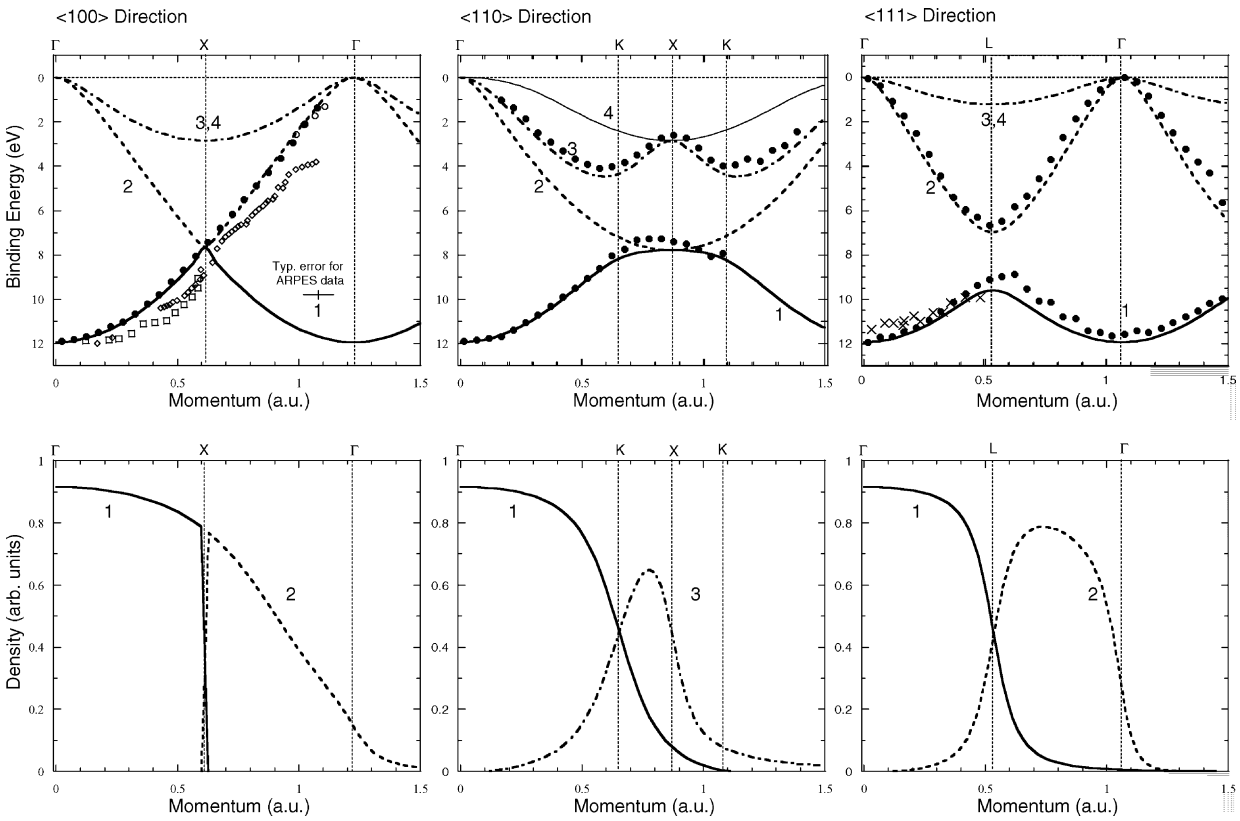

Fig. 6. The calculated dispersion (lines) and that obtained from the EMS data (dots) along the three different symmetry directions along with some photoemission data (the open circles are ARPES data from ref. [16] and the diamonds, squares and crosses are ARPES data from [17]). In the bottom three panels we show the calculated momentum density for these three cases, split up in the contribution of the different bands, as indicated with the numbers and line-styles.

may change by elastic scattering with a probability that is reflected in the observed intensity. The momentum scale of these figures are calibrated using the known position of the diffracted single crystal peaks. A more quantitative assessment of these diffraction pictures is planned, taking into account saturation effects of the phosphorous/camera combination, and these pictures should presently be interpreted only semi-quantitatively. However, it is clear that the crystalline and amorphous films interact with the incoming beam quite differently.

It is interesting to compare the EMS spectra from samples that show such different diffraction behaviour. This is done in Fig. 8. Of course the results for crystalline silicon are dependent of the crystal orientation. Here we show selected spectra for both the ⟨1 0 0⟩ and ⟨1 1 0⟩ orientation, as well as the corresponding spectra for the amorphous sample. The crystalline spectra are significantly sharper, with the clear resolution of two peaks at the crossing of the first Brillouin zone in the ⟨1 1 0⟩ case and additional structures at higher momenta in the ⟨1 0 0⟩ case, corresponding to band 4 (sampled due to finite momentum resolution, as the measurement line skirts the 4th Brillouin zone as shown in Fig. 4).

Such broadening, at least away from zero momentum, is predicted by theory. The structures shown in the calculations from Hickey and Morgan [20] have a width of 4–5 eV when convoluted with an energy resolution of 1 eV. Ziman predicts no additional broadening near zero momentum [19] but the observed peak at zero momentum seems broader in the amorphous case than in the single-crystal case. However, many-body effects such as life-time broadening, to be discussed later, could be different for amorphous Si than in single crystals.

3.3. Diffraction and the measurement of momentum densities

For amorphous materials elastic scattering causes a background to the measured momentum densities due to the broadening of the momentum distribution of the incoming and outgoing beams, as shown in the central panel of Fig. 7. It does not provide new structures and can be modelled reasonably well using Monte Carlo procedures [12]. As is clear from Fig. 7, for single crystals the incoming (as well as the outgoing) electrons are more likely to change their momenta by certain values, corresponding to reciprocal lattice vectors. These diffraction effects cause new structures, and these weak ghosts of the main structures are observed. Evidently, this cannot be modelled by Monte Carlo simulations based on atomic elastic scattering cross sections, and full understanding would require the use of the dynamical theory of

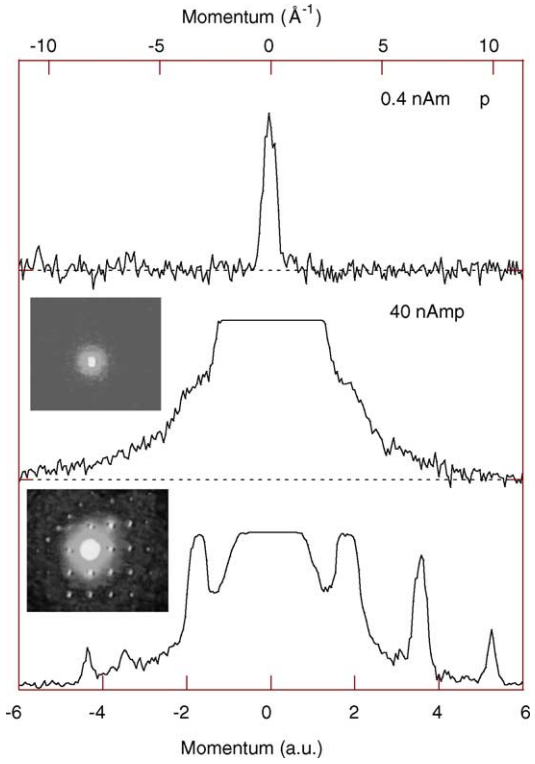

Fig. 7. The intensity distribution of the transmitted beam (50 keV) as measured on a phosphorous screen. For a thin (about 8 nm thick) amorphous silicon film the main peak is sharp (top panel), due to electrons that have not scattered elastically. Increasing the electron beam causes saturation of the main peak, but clear shoulders with some broad structure appear (centre panel), indicative of amorphous materials, due to electrons that have scattered elastically. For a single crystal of silicon we see sharp peaks, due to diffraction superimposed on a incoherent background of roughly the same shape as that of the amorphous film (lower panel). The diffraction patterns are shown in the inserts. The intensity distribution was obtained along the vertical line through the main peak of the diffraction pattern.

diffraction [21]. Here we want to show that a semi-empirical approach can remove these elastic scattering effects, at least in first order.

In Fig. 9 we show the momentum profiles for the measurement in the ⟨1 1 1⟩ direction. This measurement was done by tilting the sample as indicated in Fig. 2d. In this case the (1 1 1) reciprocal lattice vector with a length of 1.05 a.u. will affect the measurement. Indeed we see a replica of the main feature shifted by ±1.05 a.u. in these momentum distributions (see also the lower panel in Fig. 5). No theory predicts that the momentum distribution of the valence band of silicon has significant intensity beyond 2 a.u. Thus, we can safely assume that the peaks beyond 2 a.u. are due to diffraction. This allows us to establish the ratio of the intensity of the main feature and the replica. Using a single factor of the main to replica intensity ratio (one factor for the right and one for the left replica) we can now subtract the replica feature from all the momentum profiles. In this way the solid line is obtained, with momentum distributions that are close to the calculated ones, i.e. band 1 has significant intensity between 0 and 0.6 a.u. whereas band 2 is occupied from 0.4 to 1.1 a.u. (see also Fig. 6, lower right panel). Using only a single fitting parameter we removed both the high momentum branch (near $|q| = 2$, as well as the low momentum branch (with $|q| < 0.5$ a.u. of band 2, as well as the high momentum branch of band 1 ($|q| > 0.7$ a.u.).

3.4. Inelastic multiple scattering and the measurement of line shapes

Although agreement between the measurements and the FP-LMTO calculations is in general quite good, it is clear even from the semi-quantitative grey-scale presentations in Fig. 5 that there are differences in detail. The measured energy widths at a given momentum are much larger than the theoretical ones even though the experimental energy resolution has been folded into the calculations. Also the measurements show maximum intensity at intermediate energies or near the top of the band, whereas the theory predicts maximum intensity near the bottom of the band. These effects are due to lifetime broadening of the spectral momentum density due to electron correlations.

Fig. 10 shows two spectra obtained along the ⟨1 1 0⟩ direction, one at $\boldsymbol{q} \simeq 0$ near the Γ point and the other near the X point at $q \simeq 0.87$ a.u. The peak near the X point is much narrower and taller than the peak near $\boldsymbol{q} = 0$, which also is quite asymmetric. The figure shows the raw data and the data corrected in a parameter-free way for inelastic scattering, using the measured EELS spectra, as discussed earlier. This still leaves considerable density at binding energies above the main quasiparticle peaks. If one attempts to remove this extra high-energy intensity by further deconvolution one obtains non-physical negative intensities at some binding energies.

The results of full-scale many-body calculations using the GW [22] and cumulant expansion [23,24] approximations to the one-hole Green's function are compared with some of the measurements in Fig. 11 [15]. The theories, convoluted with the experimental energy resolution, are normalised to the data at one point only, namely to the peak in the quasiparticle structure at the common $\boldsymbol{q} = 0$ point, the theories having the same total density at this point. In the ⟨1 0 0⟩ direction, the small low-binding-energy peak in the measurements at intermediate q_y values is due to the picking up of intensity from band 4 as already discussed.

The GW calculation gives a peak in the satellite density at around $\varepsilon = 34$ eV at $q \simeq 0$, which is not observed in the measured data. The cumulant expansion calculation gives a better fit to the data, although both calculations significantly underestimate the satellite density. The main quasiparticle peaks are, however, well described by both models. In particular they give the broadening and asymmetric structure of the observed features quite well, although they nevertheless still underestimate the width of the quasiparticle peak, particularly at low momentum. It is this lifetime broadening which gives rise to the reduction in the peak heights at the lower momenta.

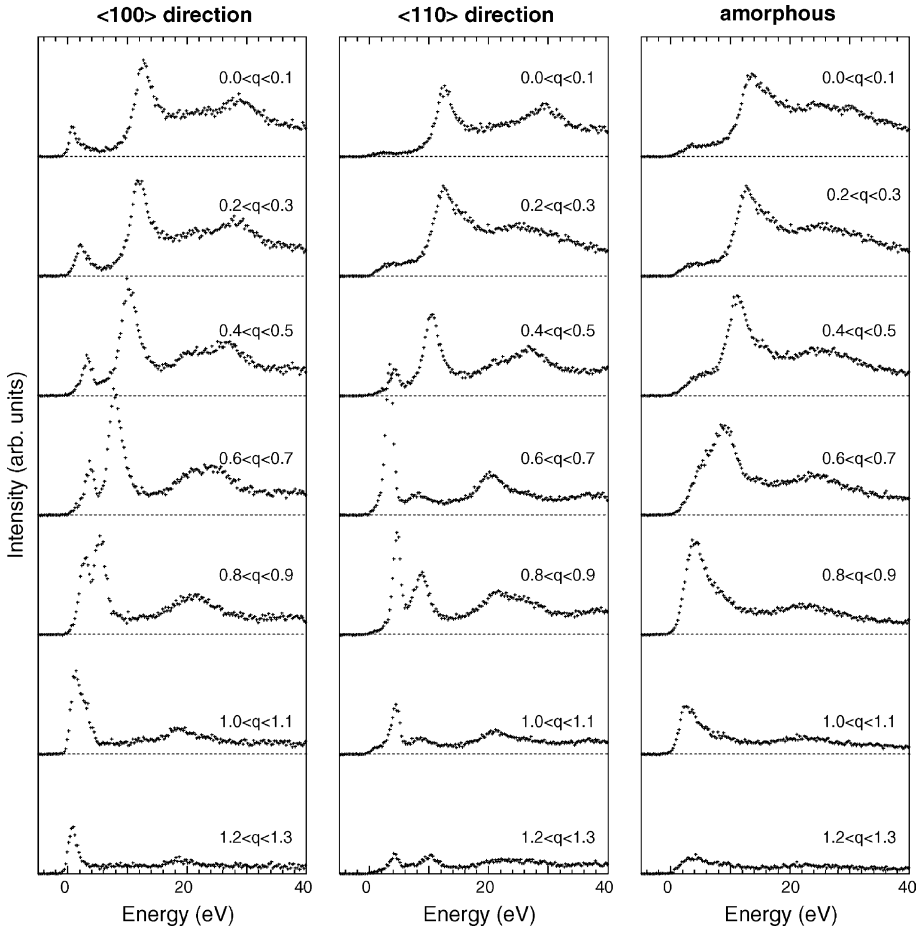

Fig. 8. The measured spectra for selected momentum intervals for single-crystal silicon film (indicated momentum in (a.u.) directed along the ⟨1 0 0⟩ (left) and ⟨1 1 0⟩ (central) direction, compared to the same spectra for an amorphous silicon film (right panel).

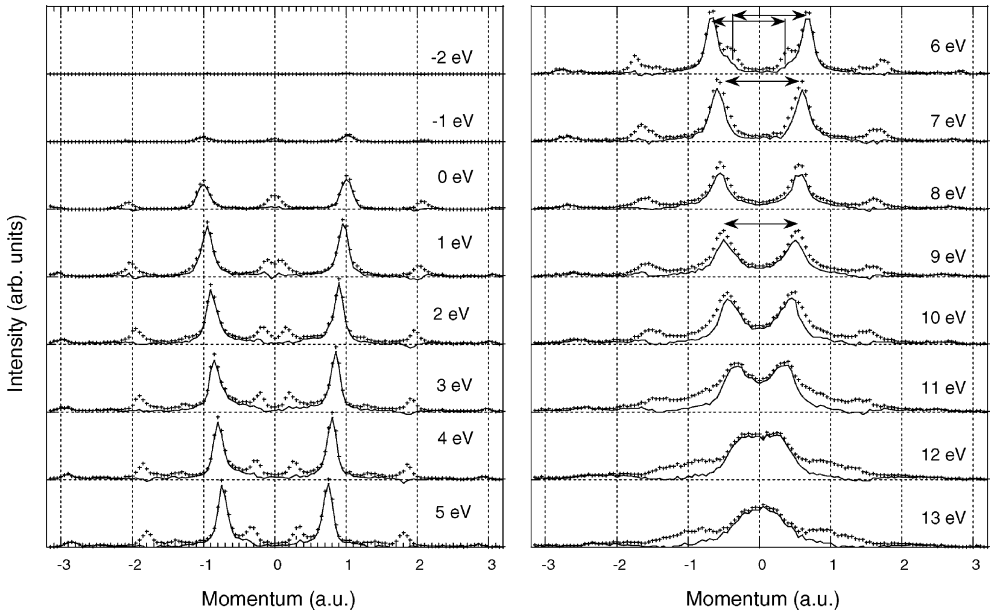

Fig. 9. The measured momentum densities, at indicated binding energy, along the ⟨1 1 1⟩ direction. The crosses are the measured distributions with diffraction effects, the solid line is the result after subtraction of the diffracted intensity, as explained in the text. The arrows indicate the length of the (1 1 1) reciprocal lattice vector. Intensity between 8 and 13 eV binding energy is from band 1, between 0 and 7 eV from band 2.

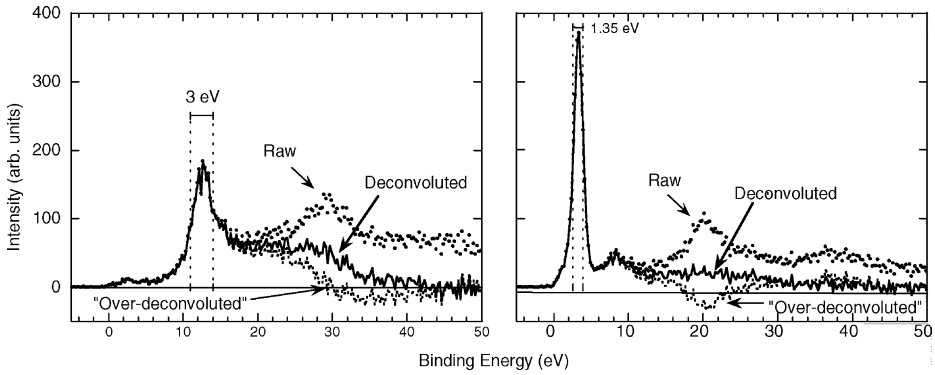

Fig. 10. EMS spectra along the ⟨1 1 0⟩ direction near $\boldsymbol{q} = 0$ (left panel) and at $q_y = 0.87$ a.u. near the X point (right). The raw data are indicated by dots and the data deconvoluted for inelastic scattering in an identical parameter-free way by the solid line. The squares show the data that have been deliberately "over-deconvoluted".

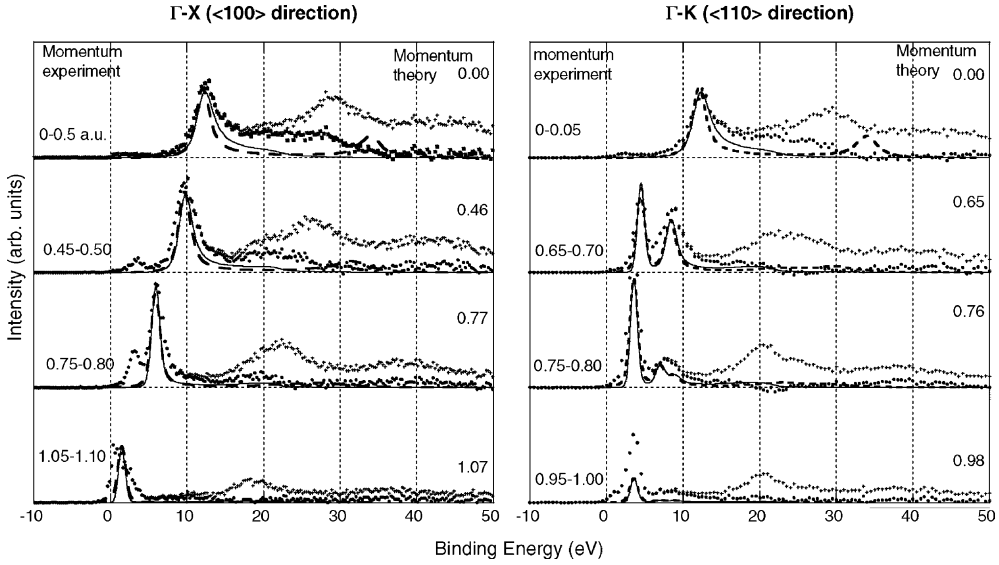

Fig. 11. EMS spectra, raw and deconvoluted, at selected momenta along the ⟨1 0 0⟩ (left) and ⟨1 1 0⟩ (right) directions. The full and dashed lines are the results of the cumulant expansion and *GW* calculations, respectively. They are normalised to the quasiparticle peak height at $\boldsymbol{q} = 0$.

4. Conclusions

We presented state-of-the-art measurements of the spectral function of both single crystal and amorphous silicon films. EMS provides access to a large range of phenomena related to the electronic structure. We have seen that it can track dispersion over a wide range of momenta. It measures real momentum and hence gives access to momentum densities when multiple scattering effects are accounted for. We have shown that this is possible, at least to a good approximation, to correct for both elastic and inelastic multiple scattering. The measurement of amorphous silicon systems shows that this technique can test theories for the electronic structure of amorphous materials in an unique way. Finally, the shape of the observed spectra can be compared to many-body calculations.

Even for silicon the number of possible measurements by EMS has not been exhausted. We plan to set up well-controlled interference conditions for the incoming beam. Under these two-beam conditions the incoming beam has different densities at different positions in the lattice. This will make energy-resolved measurements possible of distortion effects seen in Compton scattering (see e.g. [25,26]).

Since its infancy at the end of the sixties [27,28] the study of the electronic structure of solids using all-electron coincidence techniques has come a long way. The potential of the technique was quickly realised by theoretical physicists (e.g. [29]) but it has taken a lot of hard work and technological developments in the area of multi-dimensional electron analysers to fulfill its promise. Even now there are no indications that we have reached the end of the road, and with improvements in spectrometer resolution as well as better sample preparation techniques, this spectroscopy will provide increasingly stringent tests of our understanding of the electronic structure of matter.

Acknowledgements

This research is supported by the Australian Research Council.

References

[1] M.J. Cooper, Rep. Prog. Phys. 48 (1985) 415.
[2] M.J. Cooper, Radiat. Phys. Chem. 50 (1997) 63.
[3] B.G. Williams, T.G. Sparrow, R.F. Egerton, Proc. R. Soc. A 393 (1984) 409.
[4] F. Bell, J.R. Schneider, J. Phys. Condens. Matter 13 (2001) 7905.
[5] M. Itou, S. Kishimoto, H. Kawata, M. Ozaki, H. Sakurai, F. Itoh, J. Phys. Soc. Jpn. 68 (1999) 515.
[6] E. Weigold, I.E. McCarthy, Electron Momentum Spectroscopy, Kluwer Academic/Plenum, New York, 1999.
[7] M. Vos, G.P. Cornish, E. Weigold, Rev. Sci. Instrum. 71 (2000) 3831.
[8] M. Vos, E. Weigold, J. Electron Spectrosc. Relat. Phenom. 112 (2000) 93.
[9] M. Vos, A.S. Kheifets, V.A. Sashin, E. Weigold, M. Usuda, F. Aryasetiawan, Phys. Rev. B 66 (2002) 155414.
[10] R. Courths, S. Hüfner, Phys. Rep. 112 (1984) 53.
[11] M. Vos, V.A. Sashin, C. Bowles, A.S. Kheifets, E. Weigold, J. Phys. Chem. Solids, in press.
[12] M. Vos, M. Bottema, Phys. Rev. B 54 (1996) 5946.
[13] M. Vos, A.S. Kheifets, E. Weigold, Correlations, polarization and ionization in atomic systems, in: D.H. Madison, M. Schulz (Eds.), AIP Conference Proceedings 604, American Institute of Physics, New York, 2002, pp. 70–75.
[14] M. Vos, A.S. Kheifets, V.A. Sashin, E. Weigold, J. Phys. Chem. Solids 64 (2003) 2507.
[15] A.S. Kheifets, V.A. Sashin, M. Vos, E. Weigold, F. Aryasetiawan, Phys. Rev. B 68 (2003) 233205.
[16] A.L. Wachs, T. Miller, T.C. Hsieh, A.P. Shapiro, T.-C. Chiang, Phys. Rev. B 32 (1985) 2326.
[17] D.H. Rich, G.E. Franklin, F.M. Leibsle, T. Miller, T.C. Chiang, Phys. Rev. B 40 (1989) 11804.
[18] M. Vos, P. Storer, Y. Cai, A. Kheifets, I. McCarthy, E. Weigold, J. Phys. Condens. Matter 7 (1995) 279.
[19] J. Ziman, J. Phys. C Solid State Phys. 4 (1971) 3129.
[20] B. Hickey, G. Morgan, J. Phys. C Solid State Phys. 19 (1986) 6195.
[21] L.J. Allen, I.E. McCarthy, V.W. Maslen, C.J. Rossouw, Aust. J. Phys. 43 (1990) 453.
[22] L. Hedin, S. Lundqvist, Solid State Phys. 23 (1969) 1.
[23] F. Aryasetiawan, L. Hedin, K. Karlsson, Phys. Rev. Lett. 77 (1996) 2268.
[24] M. Vos, A.S. Kheifets, E. Weigold, S.A. Canney, B. Holm, F. Aryasetiawan, K. Karlsson, J. Phys. Condens. Matter 11 (1999) 3645.
[25] W. Schülke, U. Bonse, S. Mourikis, Phys. Rev. Lett. 47 (1981) 1209.
[26] J.A. Golovchenko, D.R. Kaplan, B. Kincaid, R. Levesque, A. Meixner, M.F. Robbins, J. Felsteiner, Phys. Rev. Lett. 46 (1981) 1454.
[27] U. Amaldi Jr., A. Egidi, R. Marconero, G. Pizzella, Rev. Sci. Instrum. 40 (1969) 1001.
[28] R. Camilloni, A.G. Guidoni, R. Tiribelli, G. Stefani, Phys. Rev. Lett. 29 (1972) 618.
[29] V. Levin, V. Neudachin, Y.F. Smirnov, Phys. Status Solidi (b) 49 (1972) 489.